Fast High-Efficiency Photon-Number-Resolving Parallel Superconducting Nanowire Single-Photon Detector

Stasi, Lorenzo; Gras, Gaétan Daniel Michel; Berrazouane, Riad; Perrenoud, Matthieu; Zbinden, Hugo; Bussieres, Félix

How to cite

STASI, Lorenzo et al. Fast High-Efficiency Photon-Number-Resolving Parallel Superconducting Nanowire Single-Photon Detector. In: Physical review applied, 2023, vol. 19, n° 6, p. 1–8. doi: 10.1103/PhysRevApplied.19.064041

This publication URL: https://archive-ouverte.unige.ch/unige:170225

Publication DOI: 10.1103/PhysRevApplied.19.064041

Fast High-Efficiency Photon-Number-Resolving Parallel Superconducting Nanowire Single-Photon Detector

Lorenzo Stasi,[1,2,*] Gaëtan Gras,[1] Riad Berrazouane,[1] Matthieu Perrenoud,[2] Hugo Zbinden,[2] and Félix Bussières[1]

[1] *ID Quantique SA, CH-1227 Carouge, Switzerland*

[2] *Group of Applied Physics, University of Geneva, CH-1211 Geneva, Switzerland*

(Received 29 July 2022; revised 12 October 2022; accepted 5 May 2023; published 13 June 2023)

Photon-number-resolving (PNR) single-photon detectors are an enabling technology in many areas, such as photonic quantum computing, nonclassical light-source characterization, and quantum imaging. Here, we demonstrate high-efficiency PNR detectors using a parallel superconducting nanowire single-photon-detector (P-SNSPD) architecture that does not suffer from crosstalk between the pixels and that is free of latching. The behavior of the detector is modeled and used to predict the possible outcomes given a certain number of incoming photons. We apply our model to a four-pixel P-SNSPD with a system detection efficiency of 92.5%. We also demonstrate how this detector allows reconstructing the photon-number statistics of a coherent source of light, which paves the way towards the characterization of the photon statistics of other types of light source using a single detector.

DOI: 10.1103/PhysRevApplied.19.064041

I. INTRODUCTION

Quantum states of light are made of a superposition of photon-number states. This is at the core of quantum optics and all of its practical applications, such as quantum key distribution with coherent states [1–3], linear optical quantum computing based on downconverted photon pairs, or on squeezed states of light [4]. In this context, photon-number-resolving (PNR) detectors are known to play a key role in the processing itself [5]. PNR detectors are also beneficial in several other fields, such as the characterization of quantum sources of light [6] and imaging with threshold detectors [7]. PNR detectors have been realized using different platforms [8]. Among these, transition-edge sensors (TESs) [9] have so far demonstrated impressive performances in terms of combined efficiency and single-shot measurement fidelity [10,11] thanks to their bolometric working principle. Photon-number resolution with TESs, however, has shortcomings, such as long recovery times (approximately μs), high jitters ($\sim$ns), and very low operating temperatures (between 50–100 mK). This currently prevents their use in high-repetition rate experiments and impairs the scalability of optical quantum processors.

Interestingly, these shortcomings can potentially be overcomed by superconducting nanowire single-photon detectors (SNSPDs), as they can have short recovery times ($\leq$10 ns) [12] and low jitters (as low as a few ps) [13–15]. They can also have near-unity efficiency [16] and very low dark-count rates. Due to their working principle based on hot-spot creation, SNSPDs do not however possess intrinsic photon-number resolution capability in the same way TESs do. To achieve some degree of resolution, one has to resort to other approaches. One is to exploit the fact that several simultaneous hot spots can change the detector signal's slew rate [17,18] or amplitude when using impedance-matched tapers [19]. These methods can yield discrimination up to three-photon events and can help to discriminate one versus more than one photon pulses to improve the autocorrelation function of heralded photons [20,21]. However, their resolution power quickly fades because with three or more photons absorbed, the overlap of the different signals makes the photon-number discrimination impossible.

To get more information about the number of absorbed photons, one can exploit multiplexing, either spatially with multipixel SNSPDs or temporally with delay lines [22,23]. Spatial multiplexing with several pixels to approach linear photon-number resolution, each connected to its own coaxial lines was demonstrated recently [24]. This can be simplified using a parallel SNSPD (P-SNSPD) design where the pixels are connected in parallel to a single coaxial line, and the signal's amplitude provides information on the number of pixels that clicked [25–27]. This P-SNSPD approach provides a path towards high-efficiency, low-jitter, and short recovery time PNR detectors, as it offers a mean to probe the statistics of quantum light using a single device. Ultimately, P-SNSPDs have the potential to allow single-shot high-fidelity identification of the

*Corresponding author. lorenzo.stasi@idquantique.com

incident photon number approaching the capability of the TES detector [28]. Here we take a step in this direction by showing a high-performance P-SNSPD device and by using it to probe and reconstruct the statistics of quantum light.

II. P-SNSPD MODEL

A P-SNSPD is a set of individual SNSPD pixels that are connected in parallel. They are biased by the same current source and are illuminated such that each pixel receives a portion of the incident light, and each pixel has its own detection efficiency. When one or several pixels click simultaneously, the output signal's amplitude is proportional to the number of pixels that clicked. Here, we assume that the amplitudes are discrete and perfectly distinguishable, and that there is no instantaneous crosstalk between them. We wish to develop a model of a P-SNSPD that can allow one to map the input statistics of the light to the output signals produced by the device. This has been attempted previously in Refs. [26,27] where assumptions, such as the same efficiency for each pixel or a uniform spacial distribution of light are taken. These assumptions generally do not hold in practice, but are useful to achieve the reconstruction of input light statistics. Another approach is to use quantum detector tomography [18,29] where the underlying details of the device does not need to be modeled. While this approach can work, it does not reveal some interesting details about the device itself, such as different efficiencies between the pixels. The approach we take here does not make any prior assumption on the pixel efficiencies but allows us to estimate them. Furthermore, our approach requires only one set of data to fully characterize the device and is fast to implement.

Let us consider a P-SNSPD illuminated by a photon-number distribution that we write as a column vector $\mathbf{S}$, where each element is written as S_m and is the probability to have m photons incident on the detector. Let $\mathbf{Q}$ be a column vector with elements Q_n representing the probability to observe each of the possible discrete amplitudes of the output signal, where $n = \{0, 1, \ldots, N\}$ with N equal to the number of pixels. We denote the amplitude of n pixels clicking as an n click. We wish to find the matrix $\mathbf{P}$ that maps the input photon-number distribution $\mathbf{S}$ into the n-click probability distribution $\mathbf{Q}$ through the relation $\mathbf{Q} = \mathbf{PS}$. Elementwise, the relation is expressed as

$$Q_n = \sum_{m=0}^{\infty} P_{nm} \times S_m, \tag{1}$$

where P_{nm} is the probability of registering an n click when m photons are incident. We note that the probabilities P_{nm} can be used to define the elements of the positive-operator-valued measures (POVMs) of the detector [30].

While the m can, in principle, take an infinite value, in practice, it can be truncated to finite values. All the P_{nm} elements with $n > m$ are set to 0, and if we truncate m to the value M, then $\mathbf{P}$ takes the form:

$$\mathbf{P} = \begin{bmatrix} P_{00} & P_{01} & P_{02} & \cdots & P_{0M} \\ 0 & P_{11} & P_{12} & \cdots & P_{1M} \\ \vdots & \vdots & \ddots & \cdots & \vdots \\ 0 & 0 & 0 & P_{nn} & P_{nM} \end{bmatrix}. \tag{2}$$

To construct each element of the matrix $\mathbf{P}$, we enumerate all the possible cases as if the photons in the incident pulse are registered one at a time. Thus, for a specific m photons with n-click event, we take into account two kinds of combinations: which photons are absorbed in the group of m, and which pixels detected them.

As free parameters, we use the single-pixel efficiencies η_i, which are composed by the product of the internal quantum efficiency and the coupling efficiency between the fiber and the pixel. The latter is needed in order to consider that each pixel could receive a different portion of light with respect to the others. See Appendix A for more details.

III. RESULTS

We fabricate a four-pixel P-SNSPD based on amorphous MoSi as the superconducting material using a process outlined in Ref. [12]. The superconducting layer is 6 nm thick, each pixel has 120-nm-wide nanowires with a fill factor of 0.6 covering an active area of $16 \times 16\,\mu\text{m}^2$ (see Fig. 1) and light is fiber coupled to the detector via a self-alignment packaging [31].

The particular architecture presented in this paper prevents the electrical crosstalk. The thermal crosstalk is avoided by engineering a gap between the pixels.

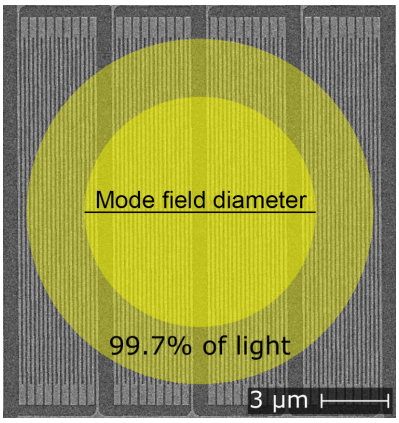

FIG. 1. SEM image of the active area of a 4-pixels P-SNSPD with the mode field diameter dimension of 1550 nm single-mode fiber on top. The active area covers $16 \times 16\,\mu\text{m}^2$.

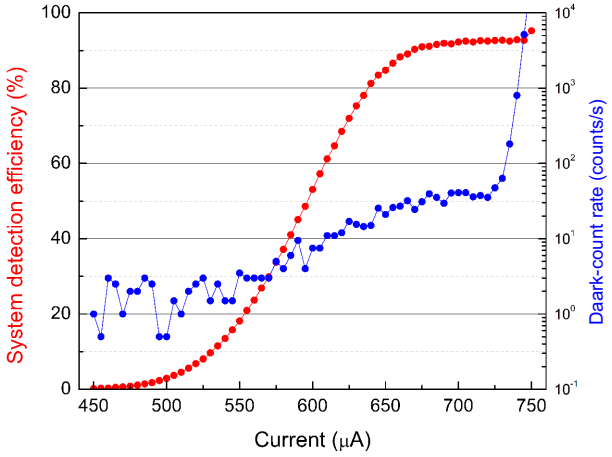

FIG. 2. System detection efficiency and system dark counts as a function of bias current for a four-pixel P-SNSPD, measured at 0.8 K.

We characterize the system detection efficiency (SDE) in a three-stage cryostat at 0.8 K by using a calibrated powermeter and three variable digital attenuators. The light polarization is oriented in order to maximize the SDE. In Fig. 2, the SDE *vs* bias current is shown at a detection rate of approximately 100 kHz. The presence of a plateau indicates the saturated internal quantum efficiency of the device and the maximum value is $92.5 \pm 2.4\%$. Dark-count rate (DCR) remains negligible along the plateau, around 140 counts/s. The DCR of the system alone, namely without the fiber plugged into the cryostat, are around 35 counts/s.

The recovery of the efficiency after a detection is directly measured by shining CW light and by measuring the probability distribution of the time between two

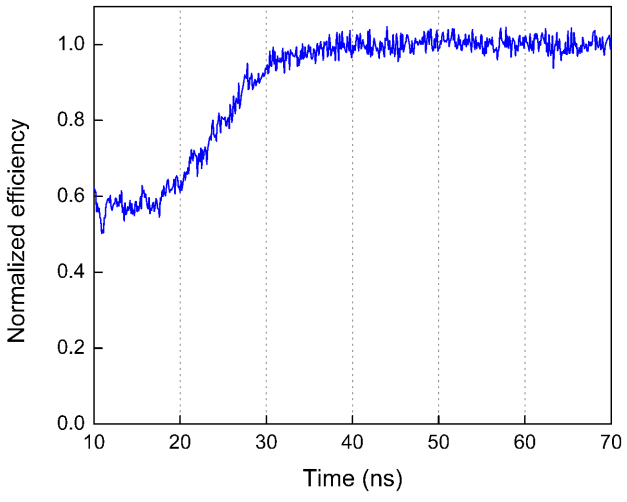

FIG. 3. Recovery time of a four-pixel P-SNSPD. The detector already displays more than 50% nominal efficiency after only 10 ns and the efficiency has fully recovered after 40 ns.

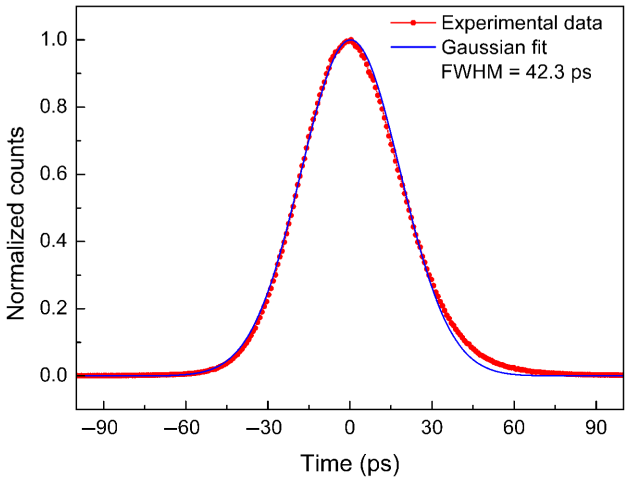

FIG. 4. Jitter of the four-pixel P-SNSPD. It is measured with a 6-ps pulsed laser at a detection rate of approximately 10^5 counts/s.

detections (see Fig. 3). After a single-photon absorption by one of the pixels, the latter becomes inactive, but the overall device is still able to detect new incoming photons due to the three other active pixels. In fact, the P-SNSPD displays more than 50% of its nominal efficiency after 10 ns and it is back at full efficiency in 40 ns.

Another feature of SNSPDs is their timing jitter. For the P-SNSPD, the curve shows a Gaussian shape, which indicates that the parallel design does not seem to affect the timing jitter of the detector when compared to a standard single-pixel detector. We obtain a jitter of 42 ps at FWHM at the single-photon level (see Fig. 4), a relatively higher result with respect to state-of-the-art SNSPDs. The reason is due to the current redistribution among the outer pixels, which cause less current into the read-out circuit reducing the signal-to-noise ratio and thus increasing the jitter.

Such results show how the P-SNSPDs can maintain high SDE, low DCR, and low jitter similar to a single meander SNSPDs, displaying a fast recovery time with more than 50% nominal efficiency after only 10 ns and the additional feature of PNR capability.

A. Probabilities matrix

In the P-SNSPDs architecture, each pixel is connected to the other, thus they cannot be read out individually. Therefore, it is not possible to compute **P** directly, since it is a function of the single-pixel efficiencies $\{\eta_i\}$.

In order to obtain **P**, we characterize the PNR capabilities of our detector with a known light source of input statistics **S** and we record the statistics generated by the detector **Q**. Then we use an optimization algorithm that finds the pixel efficiencies minimizing the Euclidean norm

$$\|\mathbf{Q} - \mathbf{PS}\|_2. \tag{3}$$

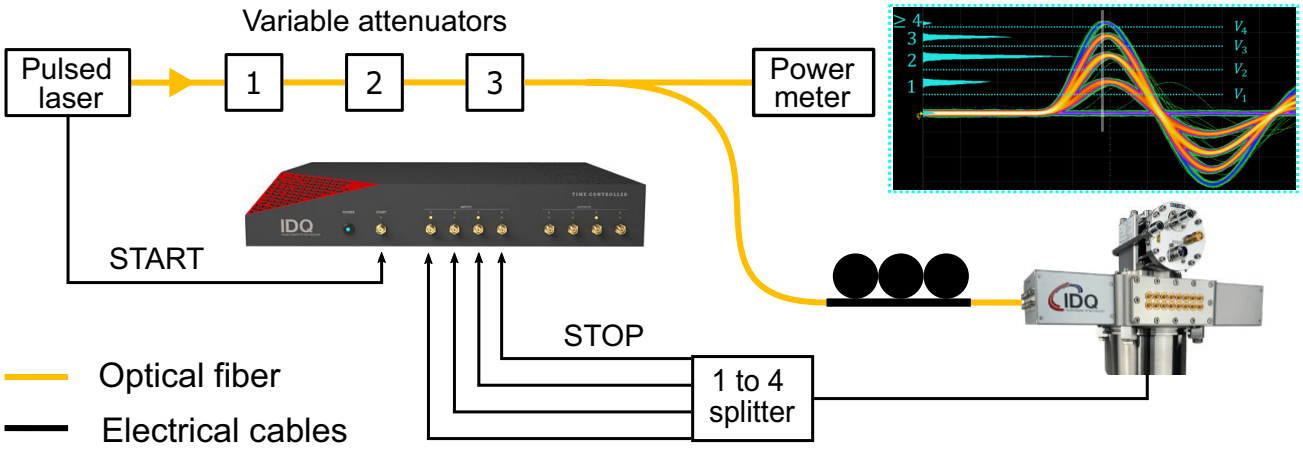

FIG. 5. Schematic of the experiment's setup. Pulsed light (10 MHz) is shone onto the detector and the generated electrical signal is sent to a 1-to-4 resistive splitter before going to the time tagger. On each input, different voltage thresholds (V_1 to V_4) are set to obtain the corresponding click events as shown on the top-right inset.

As input statistics S_m, we use Poissonian light:

$$S_m = \frac{\mu^m}{m!} e^{-\mu}, \tag{4}$$

where μ is the mean photon number per pulse.

The output statistics Q_n is measured as follows, exploiting the setup in Fig. 5.

(i) A pulsed laser (ID3000 from ID Quantique) is triggered at 10-MHz repetition rate, sending a light pulse (22 ps) to the detector and an electrical one to the time tagger (ID900 from ID Quantique). The latter serves as the start signal to build histograms for each photon event.

(ii) The electrical signal coming from the detector is sent to a 1-to-4 resistive splitter (ZFRSC-4-842-s+ Mini-Circuits) and then to the time tagger as the stop signal for the histograms. Different thresholds are set on each input, corresponding to 1-, 2-, 3-, and 4-photon events. The counts are taken in a 2-ns window. Counts contributing to a photon-number event are also contained in the counts of a lower photon-number event, hence the real counts for a specific event are $c'_n = c_n - c_{n+1}$.

(iii) To obtain the 0-photon event, we subtract from the total number of events, the registered ones. The total number of events is computed as $N_{\text{tot}} = R \times t$ where R is the repetition rate of the laser and t the time of acquisition, which is set on the ID900 to be 1 min.

Thanks to our design that prevents electrical and thermal crosstalk, and the negligible DCR (the probability to have a dark count in the time window of the experiment is 2.8×10^{-7}), we validate the model assumptions of setting to 0 all the P_{nm} elements with $n > m$. In the case that DCR would be non-negligible, the model can be adapted to consider such an effect.

We acquire several sets of data at different μ using a powermeter and three digital optical attenuators. We span μ from 0.1 to 2 (leading to a photon flux between 10^6 and 2×10^7 photons/s) and the probability matrices obtained are in agreement with each other.

The retrieved pixel efficiencies are $2.48 \pm 0.06\%$, $35.65 \pm 0.87\%$, $48.62 \pm 1.18\%$, and $5.66 \pm 0.14\%$. The data reflect the Gaussian distribution of light in single-mode fibers, with the outer pixels showing a much lower efficiency compared to the central ones. From those values, we reconstruct **P** and obtain the fidelity probabilities P_{nn}. We limit the matrix dimension to $M = 9$ during the optimization process, in order to take into account more than 99.99 % of the events generated by the Poissonian light source. In Eq. (5) we report **P** and in Eq. (6) the uncertainty values for each P_{nm} element with two significant digits. The elements in **P** are rounded to have the same decimal digits of the $\sigma_{\mathbf{P}}$ elements.

$$\mathbf{P} = \begin{bmatrix} 1 & 0.076 & 0.0063 & 0 & 0 & 0 & 0 & 0 & 0 & 0 \\ 0 & 0.924 & 0.507 & 0.260 & 0.135 & 0.0716 & 0.0383 & 0.0207 & 0.0113 & 0.0062 \\ 0 & 0 & 0.487 & 0.647 & 0.6728 & 0.6482 & 0.6067 & 0.5596 & 0.5139 & 0.4712 \\ 0 & 0 & 0 & 0.0919 & 0.1858 & 0.2645 & 0.3275 & 0.3777 & 0.4177 & 0.4498 \\ 0 & 0 & 0 & 0 & 0.00588 & 0.0157 & 0.0281 & 0.0419 & 0.0569 & 0.0767 \end{bmatrix}, \tag{5}$$

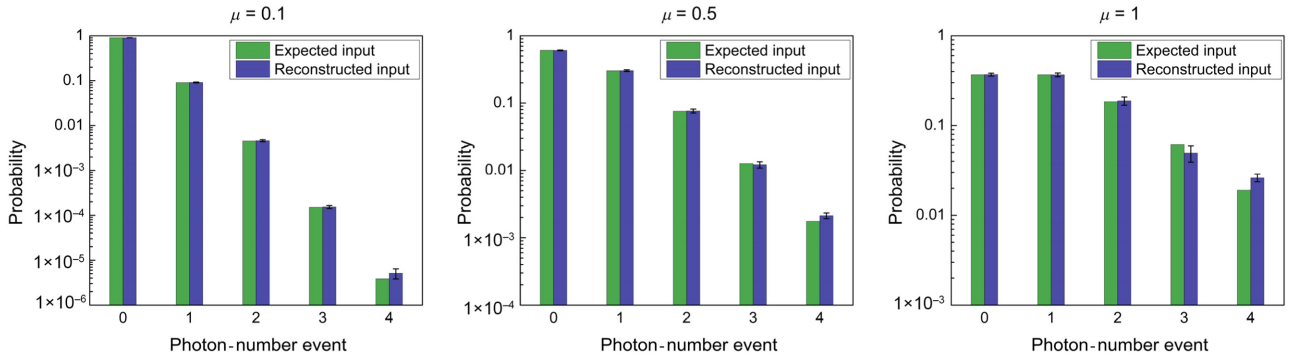

FIG. 6. Comparison between the expected light statistics sent onto the detector and the reconstructed one for $\mu = 0.1$ (left), $\mu = 0.5$ (center), $\mu = 1$ (right).

$$\sigma_{\mathbf{P}} = \begin{bmatrix} 0 & 0.022 & 0.0035 & 0 & 0 & 0 & 0 & 0 & 0 & 0 \\ 0 & 0.022 & 0.020 & 0.018 & 0.012 & 0.0078 & 0.0049 & 0.0030 & 0.0018 & 0.0011 \\ 0 & 0 & 0.024 & 0.012 & 0.0026 & 0.0030 & 0.0061 & 0.0079 & 0.0088 & 0.0093 \\ 0 & 0 & 0 & 0.0067 & 0.0091 & 0.0095 & 0.0092 & 0.0085 & 0.0078 & 0.0070 \\ 0 & 0 & 0 & 0 & 0.00057 & 0.0012 & 0.0018 & 0.0024 & 0.0029 & 0.0035 \end{bmatrix}. \quad (6)$$

The computation of the uncertainties can be found in Appendix B. The P_{11} reflects the SDE obtained with continuous-wave laser, proving that the model is consistent with the previous measurement. The drop in fidelity by P_{33} and P_{44} is due to two main factors:

(a) the probability that all the photons are split on different pixels decreases, therefore two photons can end up on the same pixel and only one will be detected;

(b) even if all the photons are split on different pixels, all of them have to click to register the corrected event.

Once **P** is computed, we can use it to reconstruct the statistics of unknown light sources [32,33]. We need to invert Eq. (1) to retrieve **S**, the light statistics, hence **P** needs to be square to be invertible. Since the matrix has dimension $(N + 1) \times M$, we need to reduce its dimension by truncating it. Hence, by neglecting all the P_{nm} elements with $m > N$, we are able to reconstruct only light-source statistics in which events with more than N photons are negligible, thus when μ is low. In Fig. 6 we report the reconstructed statistics of Poissonian light with three different μ values: for μ equal to 0.1 and 0.5 there is a very good agreement. At $\mu = 1$ the reconstruction starts to deviate from the theoretical input, since events with more than N photons start to be non-negligible. In fact, the detector saturates when more than N photons are impinging on it and we lose information about those higher photon-number events. To overcome this limitation, P-SNSPDs with a higher number of pixels would allow for a more accurate state reconstruction and provide better fidelity probabilities [28].

IV. CONCLUSION

In conclusion, we develop a general model that can be used to characterize the multiphoton absorption probabilities for any multipixel SNSPDs. The model is based on the possible combination of clicking pixels for a specific photon-absorption event and we do not make any assumption on the single-pixel efficiencies and neither on the light spatial distribution on the detector. We employ the model on a highly efficient and fast four-pixel P-SNSPD that displays properties comparable to commercial single-meander SNSPDs but with the extra feature of PNR capability and faster recovery time. Thanks to the model, we are able to access the fidelity probabilities of the detector, additional information that could not be characterized before, and the full P_{nm} matrix that can be used to reconstruct the statistics of unknown light sources. At the moment we are limited by the low number of pixels, but P-SNSPD seems a promising solution to overcome TES limitations. However, the number of pixels cannot grow indefinitely, since the voltage difference between the n-click events would become too small to be resolved. Improvement in the design, such as interleaved nanowires, could improve the fidelity probabilities of P-SNSPD, making them a useful tool in optical quantum computation and quantum metrology.

ACKNOWLEDGMENTS

We thank Giovanni V. Resta and Valentin Brisson for useful discussions. L.S. is part of the AppQInfo MSCA ITN, which received funding from the EU Horizon 2020 research and innovation program under the Marie Sklodowska-Curie Grant Agreement No. 956071.

APPENDIX A

In this Appendix, we detail the expression for all the P_{nm} values in the matrix **P**. Since we are considering that the photons are registered one at the time, it is straightforward to compute the P_{nm} elements keeping the number of clicks fixed, while letting the number of incident photons m be variable.

To generate a 0-click event, the detector must not click m times, therefore the P_{0m} can be written as

$$P_{0m} = \left(1 - \sum_{i=1}^{N} \eta_i\right)^m . \tag{A1}$$

The other P_{nm} are constructed as follows (see Fig. 7):

(a) the detector misses the first $\gamma^{(1)} - 1$ photons with probability $\left(1 - \sum_{i=1}^{N} \eta_i\right)^{\gamma^{(1)}-1}$;

(b) it detects the $\gamma^{(1)}$th photon generating the first click with probability $\sum_{i=1}^{N} \eta_i$;

(c) it can miss photons for other $\gamma^{(2)} - \gamma^{(1)} - 1$ times with probability $\left(1 - \sum_{\substack{j=1 \\ j \text{ active}}}^{N} \eta_j\right)^{\gamma^{(2)}-\gamma^{(1)}-1}$, where we sum over the remaining active pixels j after the first detection;

(d) it detects the $\gamma^{(2)}$th photon generating the second click with probability $\sum_{\substack{j=1 \\ j \text{ active}}}^{N} \eta_j$ where we sum over the remaining active pixels j after the first detection;

(e) we iterate such an operation depending on the n-click event we consider;

(f) after the last photon is detected, the remaining photons will be missed with probability $\left(1 - \sum_{\substack{k=1 \\ k \text{ active}}}^{N} \eta_k\right)^{m-\gamma^{(n)}}$.

By enumerating all the possible configurations of absorbed photons within the m group and all the possible combinations of clicking pixels, we can obtain the P_{nm} elements.

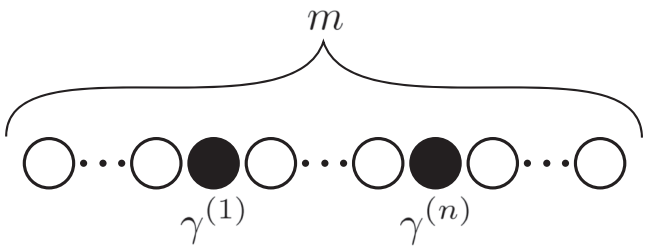

FIG. 7. Schematic representation of a string of photons arriving one at a time on the detector. The black circle indicates the position of the photon within the m group that made the detector click, whereas the white circles represent the nondetected photons.

$$P_{1m} = \sum_{1 \le \gamma^{(1)} \le m}^{m} \left\{ \left(1 - \sum_{i=1}^{N} \eta_i\right)^{\gamma^{(1)}-1} \sum_{i=1}^{N} \eta_i \left(1 - \sum_{\substack{j=1, \\ j \text{ active}}}^{N} \eta_j\right)^{m-\gamma^{(1)}} \right\}, \tag{A2}$$

$$P_{2m} = \sum_{1 \le \gamma^{(1)} < \gamma^{(2)} \le m}^{m} \left\{ \left(1 - \sum_{i=1}^{N} \eta_i\right)^{\gamma^{(1)}-1} \left\{ \sum_{i=1}^{N} \eta_i \left(1 - \sum_{\substack{j=1, \\ j \text{ active}}}^{N} \eta_j\right)^{\gamma^{(2)}-\gamma^{(1)}-1} \left[\sum_{\substack{j=1, \\ j \text{ active}}}^{N} \eta_j \left(1 - \sum_{\substack{k=1, \\ k \text{ active}}}^{N} \eta_k\right)^{m-\gamma^{(2)}} \right] \right\} \right\}, \tag{A3}$$

$$P_{3m} = \sum_{1 \le \gamma^{(1)} < \gamma^{(2)} < \gamma^{(3)} \le m}^{m} \left\{ \left(1 - \sum_{i=1}^{N} \eta_i\right)^{\gamma^{(1)}-1} \left\{ \sum_{i=1}^{N} \eta_i \left(1 - \sum_{\substack{j=1, \\ j \text{ active}}}^{N} \eta_j\right)^{\gamma^{(2)}-\gamma^{(1)}-1} \right.\right.$$
$$\left.\left. \times \left\{ \sum_{\substack{j=1, \\ j \text{ active}}}^{N} \eta_j \left(1 - \sum_{\substack{k=1, \\ k \text{ active}}}^{N} \eta_k\right)^{\gamma^{(3)}-\gamma^{(2)}-1} \left[\sum_{\substack{k=1, \\ k \text{ active}}}^{N} \eta_k \left(1 - \sum_{\substack{h=1, \\ h \text{ active}}}^{N} \eta_h\right)^{m-\gamma^{(3)}} \right] \right\} \right\} \right\}, \tag{A4}$$

$$P_{4m} = \sum_{1\le\gamma^{(1)}<\gamma^{(2)}<\gamma^{(3)}<\gamma^{(4)}\le m}^{m} \left\{ \left(1-\sum_{i=1}^{N}\eta_i\right)^{\gamma^{(1)}-1} \left\{ \sum_{i=1}^{N}\eta_i \left(1-\sum_{\substack{j=1,\\ j\ \text{active}}}^{N}\eta_j\right)^{\gamma^{(2)}-\gamma^{(1)}-1} \right.\right.$$
$$\times \left\{ \sum_{\substack{j=1,\\ j\ \text{active}}}^{N}\eta_j \left(1-\sum_{\substack{k=1,\\ k\ \text{active}}}^{N}\eta_k\right)^{\gamma^{(3)}-\gamma^{(2)}-1} \left[\sum_{\substack{k=1,\\ k\ \text{active}}}^{N}\eta_k \left(1-\sum_{\substack{h=1,\\ h\ \text{active}}}^{N}\eta_h\right)^{\gamma^{(4)}-\gamma^{(3)}-1} \right.\right.$$
$$\left.\left.\left.\left.\left.\times \left[\sum_{\substack{h=1,\\ h\ \text{active}}}^{N}\eta_h \left(1-\sum_{\substack{l=1,\\ l\ \text{active}}}^{N}\eta_l\right)^{m-\gamma^{(4)}} \right] \right] \right\} \right\} \right\}. \tag{A5}$$

APPENDIX B

The sources of error in our setup come from the power meter (PM), the 99/1 optical coupler (OP), and the three variable attenuators (ATs). To assess the uncertainty on the power meter, we measure the laser power with five different power meters of the same model and we find that the standard deviation is 2.52%.

For the optical coupler, we measure the ratio between the two output power several times and the uncertainty is 0.19%.

The attenuators are recalibrated each measurement using the powermeter by measuring the ratio between P_{AT}/P_0, where P_{AT} is the power value when the attenuation is on, and P_0 is the power value when the attenuation is zero. Therefore, the only contribution for the variable attenuators is represented by their repeatability and is measured to be 0.12%.

To compute the overall uncertainty on the total number of photons per second N_γ sent on the detector, we use the equation presented in Ref. [14]:

$$\left(\frac{\sigma_{N_\gamma}}{N_\gamma}\right)^2 = \left(\frac{\sigma_{\mathrm{PM}}}{P_{\mathrm{PM}}}\right)^2 + \left(\frac{\sigma_{\mathrm{OP}}}{R_{\mathrm{OP}}}\right)^2 + 3\left(\frac{\sigma_{\mathrm{AT}}}{\mathrm{AT}}\right)^2, \tag{B1}$$

where P_{PM} is the power read by the power meter, R_{OP} is the measured value of the 99/1 optical coupler, AT is the attenuation value and the σ_i the associated uncertainties.

Since we cannot use error propagation throughout the optimization algorithm we carry out Monte Carlo simulations to estimate the error on each P_{nm} elements. Therefore, we construct several simulated sets of data, with the following method:

(i) to obtain the alternative number of counts for a specific n-click event, we randomly toss a coin N_t times with the probability of success given by the experimental photon-number distribution Q_n recorded by the detector. The number of successful events correspond to the alternative number of n-click events. The 0-click events are obtained by subtracting from N_t the 1-, 2-, 3-, and 4-click events, to ensure that Q'_n is normalized.

(ii) The error associated to the input light statistics S_m is given by σ_{N_γ} and it is found to be 2.53%. Thus, to construct the alternative input light statistics S'_m, we randomly choose a mean photon number per pulse μ from a Gaussian distribution centered in μ with standard deviation $\sigma = 0.0253 \times \mu$. This other μ is then used to construct the Poissonian light input statistic S'_m.

Q'_n and S'_m are feed to the optimization algorithm that output the matrix **P**. We compute an average between the retrieved **P** and we use the standard deviation as the uncertainty on each P_{nm} value.

[1] N. Gisin, G. Ribordy, W. Tittel, and H. Zbinden, Quantum cryptography, Rev. Mod. Phys. **74**, 145 (2002).

[2] S. Pirandola, U. L. Andersen, L. Banchi, M. Berta, D. Bunandar, R. Colbeck, D. Englund, T. Gehring, C. Lupo, C. Ottaviani, *et al.*, Advances in quantum cryptography, Adv. Opt. Photonics **12**, 1012 (2020).

[3] F. Xu, X. Ma, Q. Zhang, H.-K. Lo, and J.-W. Pan, Secure quantum key distribution with realistic devices, Rev. Mod. Phys. **92**, 025002 (2020).

[4] S. Slussarenko and G. J. Pryde, Photonic quantum information processing: A concise review, Appl. Phys. Rev. **6**, 041303 (2019).

[5] E. Knill, R. Laflamme, and G. J. Milburn, A scheme for efficient quantum computation with linear optics, Nature **409**, 46 (2001).

[6] M. Von Helversen, J. Böhm, M. Schmidt, M. Gschrey, J.-H. Schulze, A. Strittmatter, S. Rodt, J. Beyer, T. Heindel, and S. Reitzenstein, Quantum metrology of solid-state single-photon sources using photon-number-resolving detectors, New J. Phys. **21**, 035007 (2019).

[7] L. Cohen, E. S. Matekole, Y. Sher, D. Istrati, H. S. Eisenberg, and J. P. Dowling, Thresholded Quantum

LIDAR: Exploiting Photon-Number-Resolving Detection, Phys. Rev. Lett. **123**, 203601 (2019).

[8] T. Aref, *et al.*, *Superconducting Devices in Quantum Optics*, edited by R. H. Hadfield and G. Johansson (Springer, 2016), https://link.springer.com/book/10.1007/978-3-319-24091-6.

[9] D. Rosenberg, A. E. Lita, A. J. Miller, and S. W. Nam, Noise-free high-efficiency photon-number-resolving detectors, Phys. Rev. A **71**, 061803 (2005).

[10] A. E. Lita, A. J. Miller, and S. W. Nam, Counting near-infrared single-photons with 95% efficiency, Opt. Express **16**, 3032 (2008).

[11] L. A. Morais, T. Weinhold, M. P. de Almeida, A. Lita, T. Gerrits, S. W. Nam, A. G. White, and G. Gillett, Precisely determining photon-number in real-time. arXiv:2012.10158 (2020).

[12] M. Perrenoud, M. Caloz, E. Amri, C. Autebert, C. Schönenberger, H. Zbinden, and F. Bussières, Operation of parallel SNSPDs at high detection rates, Supercond. Sci. Technol. **34**, 024002 (2021).

[13] I. Esmaeil Zadeh, J. W. Los, R. B. Gourgues, J. Chang, A. W. Elshaari, J. R. Zichi, Y. J. Van Staaden, J. P. Swens, N. Kalhor, A. Guardiani, *et al.*, Efficient single-photon detection with 7.7 ps time resolution for photon-correlation measurements, ACS Photonics **7**, 1780 (2020).

[14] M. Caloz, M. Perrenoud, C. Autebert, B. Korzh, M. Weiss, C. Schönenberger, R. J. Warburton, H. Zbinden, and F. Bussières, High-detection efficiency and low-timing jitter with amorphous superconducting nanowire single-photon detectors, Appl. Phys. Lett. **112**, 061103 (2018).

[15] B. Korzh, Q.-Y. Zhao, J. P. Allmaras, S. Frasca, T. M. Autry, E. A. Bersin, A. D. Beyer, R. M. Briggs, B. Bumble, M. Colangelo, *et al.*,Demonstration of sub-3 ps temporal resolution with a superconducting nanowire single-photon detector, Nat. Photonics **14**, 250 (2020).

[16] D. V. Reddy, R. R. Nerem, S. W. Nam, R. P. Mirin, and V. B. Verma, Superconducting nanowire single-photon detectors with 98% system detection efficiency at 1550 nm, Optica **7**, 1649 (2020).

[17] C. Cahall, K. L. Nicolich, N. T. Islam, G. P. Lafyatis, A. J. Miller, D. J. Gauthier, and J. Kim, Multi-photon detection using a conventional superconducting nanowire single-photon detector, Optica **4**, 1534 (2017).

[18] M. Endo, T. Sonoyama, M. Matsuyama, F. Okamoto, S. Miki, M. Yabuno, F. China, H. Terai, and A. Furusawa, Quantum detector tomography of a superconducting nanostrip photon-number-resolving detector, Opt. Express **29**, 11728 (2021).

[19] D. Zhu, M. Colangelo, C. Chen, B. A. Korzh, F. N. Wong, M. D. Shaw, and K. K. Berggren, Resolving photon numbers using a superconducting nanowire with impedance-matching taper, Nano Lett. **20**, 3858 (2020).

[20] S. I. Davis, A. Mueller, R. Valivarthi, N. Lauk, L. Narvaez, B. Korzh, A. D. Beyer, O. Cerri, M. Colangelo, K. K. Berggren, *et al.*, Improved Heralded Single-Photon Source with a Photon-Number-Resolving Superconducting Nanowire Detector, Phys. Rev. Appl. **18**, 064007 (2022).

[21] S. Sempere-Llagostera, G. Thekkadath, R. Patel, W. Kolthammer, and I. Walmsley, Reducing $g^{(2)}(0)$ of a parametric down-conversion source via photon-number resolution with superconducting nanowire detectors, Opt. Express **30**, 3138 (2022).

[22] E. A. Dauler, B. S. Robinson, A. J. Kerman, J. K. Yang, K. M. Rosfjord, V. Anant, B. Voronov, G. Gol'tsman, and K. K. Berggren, Multi-element superconducting nanowire single-photon detector, IEEE Trans. Appl. Supercond. **17**, 279 (2007).

[23] M. Fitch, B. Jacobs, T. Pittman, and J. Franson, Photon-number resolution using time-multiplexed single-photon detectors, Phys. Rev. A **68**, 043814 (2003).

[24] B. Zhang, Q. Chen, L. Zhang, R. Ge, J. Tan, X. Li, X. Jia, L. Kang, and P. Wu, Approaching linear photon-number resolution with superconductor nanowire array, Appl. Phys. B **126**, 1 (2020).

[25] A. Divochiy, F. Marsili, D. Bitauld, A. Gaggero, R. Leoni, F. Mattioli, A. Korneev, V. Seleznev, N. Kaurova, O. Minaeva, *et al.*, Superconducting nanowire photon-number-resolving detector at telecommunication wavelengths, Nat. Photonics **2**, 302 (2008).

[26] F. Marsili, D. Bitauld, A. Fiore, A. Gaggero, R. Leoni, F. Mattioli, A. Divochiy, A. Korneev, V. Seleznev, N. Kaurova, *et al.*, Superconducting parallel nanowire detector with photon number resolving functionality, J. Mod. Opt. **56**, 334 (2009).

[27] M. Moshkova, A. Divochiy, P. Morozov, Y. Vakhtomin, A. Antipov, P. Zolotov, V. Seleznev, M. Ahmetov, and K. Smirnov, High-performance superconducting photon-number-resolving detectors with 86% system efficiency at telecom range, JOSA B **36**, B20 (2019).

[28] J. Provazník, L. Lachman, R. Filip, and P. Marek, Benchmarking photon number resolving detectors, Opt. Express **28**, 14839 (2020).

[29] T. Schapeler, J. P. Höpker, and T. J. Bartley, Quantum detector tomography of a 2×2 multi-pixel array of superconducting nanowire single photon detectors, Opt. Express **28**, 33035 (2020).

[30] J. S. Lundeen, A. Feito, H. Coldenstrodt-Ronge, K. L. Pregnell, C. Silberhorn, T. C. Ralph, J. Eisert, M. B. Plenio, and I. A. Walmsley, Tomography of quantum detectors, Nat. Phys. **5**, 27 (2009).

[31] A. J. Miller, A. E. Lita, B. Calkins, I. Vayshenker, S. M. Gruber, and S. W. Nam, Compact cryogenic self-aligning fiber-to-detector coupling with losses below one percent, Opt. Express **19**, 9102 (2011).

[32] N. Lusardi, J. Los, R. Gourgues, G. Bulgarini, and A. Geraci, Photon counting with photon number resolution through superconducting nanowires coupled to a multi-channel TDC in FPGA, Rev. Sci. Instrum. **88**, 035003 (2017).

[33] E. A. Dauler, A. J. Kerman, B. S. Robinson, J. K. Yang, B. Voronov, G. Goltsman, S. A. Hamilton, and K. K. Berggren, Photon-number-resolution with sub-30-ps timing using multi-element superconducting nanowire single photon detectors, J. Mod. Opt. **56**, 364 (2009).